A 256-Element Ultrasonic Phased Array System for the Treatment of Large Volumes of Deep Seated Tissue

Douglas R. Daum and Kullervo Hynynen, *Member, IEEE*

***Abstract*—A 256-element phased array has been designed, constructed, and tested for ablative treatment of large focal volumes of deep seated tissue. The array was constructed from a 1.1-MHz, 1-3 composite piezoelectric spherical shell with a 10-cm radius of curvature and a 12-cm diameter. The array was tested to determine its electroacoustic efficiency and inter-element coupling under high acoustic power conditions. A series of in vivo porcine experiments demonstrated the ability to produce deep seated tissue lesions in thigh muscle using the large scale phased array. The array was used to heat and coagulate tissue volumes > 5 cm^3 in a single ultrasound exposure using multiple foci and temporally scanned power deposition patterns. The spatial and temporal experimental results for large, heated focal volumes correlated very well with the simulated temperature response model for homogeneous tissue. A 25-cm^3 tissue volume was coagulated in a 90-min period using overlapping large ultrasound exposures.**

I. Introduction

The ability to coagulate deep seated tissue noninvasively has several potential clinical applications. Previous research has indicated that ultrasound-induced cell death can be produced in organs such as the eye, prostate, liver, brain, kidney, bladder, breast, and heart using minimally or noninvasive applicators [1]–[8], [41]–[48]. Ultrasonic treatments can be roughly divided into four classes: 1) continuous wave (CW) thermal treatment, 2) CW cavitation treatment, 3) pulsed thermal treatment, and 4) pulsed cavitation treatment. Of these modalities, CW thermal treatment is the most well understood and controllable method of causing cell death.

The majority of in vivo experiments to coagulate tissue noninvasively using CW ultrasound has used a focused ultrasound transducer with a large aperture and a small, fixed focus. This technique is effective because it uses the large intensity gain from the aperture of the transducer to the focal position to guarantee that only tissue at the focus is damaged. However, sharp thermal gradients at the focus are necessary to ensure proper treatment of the tissue, and the small focal volume makes the treatment of large tissue volumes unreasonably time consuming [9].

Manuscript received November 23, 1998; accepted April 2, 1999. This research was funded by NIH Grant CA46627.

K. Hynynen is with the Department of Radiology, Brigham and Women's Hospital, Boston, MA 02215 (e-mail: kullervo@bhw.harvard.edu).

D. Daum is with Guidant Corp., St. Paul, MN 55112.

Several researchers have suggested the use of CW phased array applicators to increase the focal volume (for hyperthermia [10], [11] or focal surgery [12]–[14]). Unlike shock wave arrays that can steer a single focus by timing pulses to overlap simultaneously at a tissue location during propagation, CW arrays create constructive and destructive intensity patterns throughout the propagation path with the intention of electronically targeting the peak constructive intensities of one or more foci. The thermal tissue coagulation using multiple focus patterns from various arrays has been demonstrated in vivo [15]–[18].

Previous simulation studies indicate that the treatment time of large tissue volumes (>1 to 3 cm^3) could be decreased substantially using phased arrays [9], [14] and that the improved control over the acoustic field using an array with more numerous elements could improve treatment time further [19]. This could make the treatment of tumors in locations such as the breast, prostate, liver, and other locations more time effective and clinically viable. The object of this research was to confirm experimentally the simulation results from these previous studies. That is, to demonstrate that a robust, large scale, therapeutic ultrasound array can be used to coagulate large volumes of deep seated tissue in a single sonication. To accomplish this goal, a 256-element spherical-sectioned phased array was constructed using 1-3 composite piezoelectric material. The array was characterized acoustically through hydrophone scans and efficiency measurements. It was then used in a series of in vivo porcine experiments guided and monitored using magnetic resonance imaging. The in vivo results were then compared with the simulated temperature response to assess the accuracy of the treatment simulation model applied to large focal volumes.

II. Materials and Methods

A. Guidelines Followed in Array Design

A spherical-sectioned array geometry [20] was chosen for the large scale array because it has the ability to shift single foci electronically along or across the array axis and to create multiple focus patterns. The focal steering range of the array geometry is determined primarily by the center-to-center element spacing and the individual element dimensions. The intensity and shape of the generated foci are mainly a function of the array f-number and

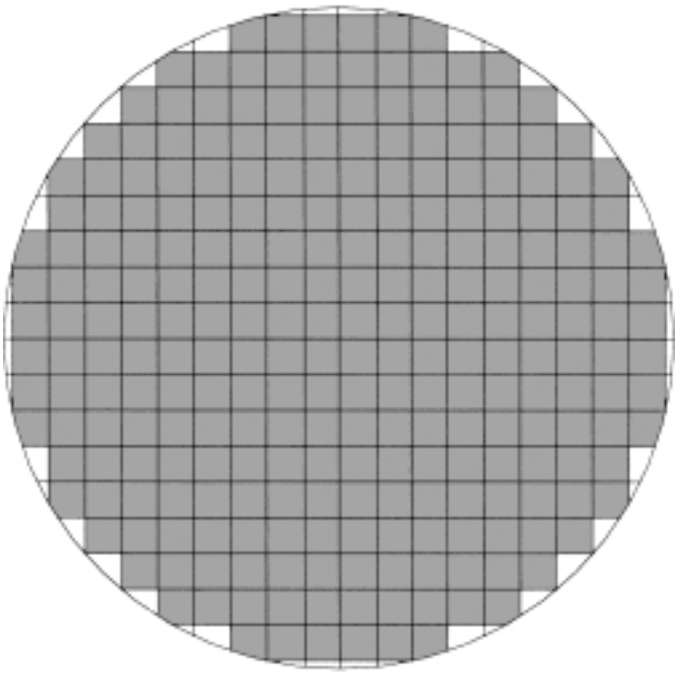

Fig. 1. Planar projection of the proposed array using the array design guidelines. The powered elements are shaded, and the small triangular spaces on the array edges were used for ground connections.

frequency. For this study, the array was designed to treat a 3-cm^3 volume in a single sonication at depths approximately 7 cm below the tissue surface. The frequency of the array was chosen to be 1.1 MHz to avoid the cavitation threshold of low frequency ultrasound and the increased attenuation of high frequency ultrasound. The f-number of the array was chosen to be < 1.0 to minimize near field heating of a single focus sonication [21]. The element size was determined by maximizing the surface area of the transducer but keeping the element projections of equal area. The array geometry (element size, element number, and frequency) was simulated to ensure that the array could shift a single focus adequately within the target volume (a 1.0×1.0-cm^2 area in the focal plane) without creating grating lobes $> 10\%$ of the main lobe. Using these parameters, the proposed array for this study contained a 10-cm radius of curvature and a 12-cm diameter with element projections of 0.65×0.65 cm^2 (see Fig. 1).

B. Numerical Simulations

The ultrasound fields of the proposed array were simulated using the Rayleigh-Sommerfeld integral over a set of geometrically superimposed point sources as described by Zemanek [22]. The acoustic vibration on the surface was modeled as uniform. The temperature elevations were calculated numerically using the Pennes bio-heat transfer equation (tissue-related parameters: perfusion = 1 kg/m^3/s, thermal conductivity = 0.48 W/m/°C, arterial blood temperature = 33.5°C, specific heat of tissue and blood = 3770 J/kg/°C, density = 998 kg/m^3, and ultrasound attenuation = 0.041 Np/cm/MHz [23], [24]), and the dose distributions were calculated from a numerical integration of the Sapareto and Dewey model [25], [26]. The equations for the simulations are found in the appendix.

In all simulations, the cross-axial spatial resolution was 0.5 mm, the along-axis spatial resolution was 1.0 mm, the temporal resolution was 0.02 s, and the region of calculation extended from 3 to 13 cm from the array and ±4 cm from the axis of the array. The large simulation volume was necessary to avoid excessive simulated cooling from the region's boundaries. To compare the simulated temperature elevations with the MR temperature images, the simulation results were averaged using a uniform spatial filter of the MR voxel size. The phase distribution for the array was calculated using the pseudoinverse technique [27]. The elements had uniform power magnitudes. All calculations were performed on a dual 300-MHz Pentium II PC (Micron, Boise, ID).

C. Preliminary Piezocomposite Array Material Characterization

Preliminary 1-3 piezocomposite material tests were performed on a flat, 9-element prototype array supplied by Imasonic (Besancon, France). This prototype array was designed to be driven at 1.0 MHz and consisted of an air-backed 3×3 grid of 0.5×0.5-cm^2 squares covered by a solid ultrasound matching layer. The elements were attached to a 1-m, 28-AWG microcoaxial cable (Belden, Richmond, IN) and electronically matched using LC circuitry to appear as a 50-Ω load to the driving system at the chosen frequency.

D. Acoustic Measurement Techniques

1. Hydrophone Scans: Automated stepper motors (Velmex, Bloomfield, NY) and a 0.075-mm hydrophone (Precision Acoustic, Dorset, England) were used to scan the array in a degassed water bath. Rubber matting was placed around the sides of the bath and hydrophone to reduce unwanted echoes. The spatial sampling was ≤ 0.2 mm.

2. Electroacoustic Efficiency Measurements: All electroacoustic efficiency measurements were made using a radiation force technique [28] with an absorbing brush and a scientific scale (Mettler Toledo AE200, Hightstown, NJ). Electrical power measurements were made for individual array elements using either an HP 438A Power Meter (Hewlett Packard, Englewood, CO) or the in-house built power meters on the ultrasound driving system [29]. Electrical power measurements delivered to the entire array simultaneously used the in-house built power meters for each individual element attached to the driving system.

3. Mechanical Coupling Measurements: Coupling measurements were made by simultaneously driving adjacent elements with the same electrical phase and then with opposite electrical phases while measuring the electrical power delivered to the elements and the radiation force

generated by the elements in each case. The decrease in output power and efficiency when the elements were driven out of phase was used as a measure of the mechanical coupling between the elements. Six adjacent elements of the prototype array and all 256 elements of the therapy array were driven to make the measurements. Individual pairs of elements were also tested.

E. Array Construction

The 256-element array was constructed from a spherically curved 1-3 piezocomposite shell (Imasonic) with a 10-cm radius of curvature and a 12-cm diameter. Although the array geometry has been titled spherical-sectioned [20], the 1-3 composite material was not sectioned by dicing through the material. The array elements were etched on the convex electrode of the array in a pattern whose planar projection is a grid of 0.65×0.65-cm^2 squares with each square being driven as an individual element (see Fig. 1). Unlike the prototype array, the front face of the transducer did not include a quarter wave acoustic matching layer. On the back of the array, one end of a small strip of silver foil was soldered directly to the element electrodes. Each element was connected to a 7-m, 34-AWG, magnet-compatible, microcoaxial cable (Precision Interconnect, Portland, OR). Electrical measurements of the cable, including the DC capacitance and conductivity, were used to estimate the piezoelement/cable impedance using a single stage L transmission line model [30]. Comparisons with the measured impedance (using an HP 4193A Vector Impedance Meter, Hewlett Packard) of the cabled transducer were made to verify the model and estimate efficiency losses in the cable. The microcoaxial cable bundle was connected to the driving system through four 156-position DL connectors (ITT Cannon, Santa Ana, CA). Each array element was matched electronically to have a 50-Ω impedance using an inductor and capacitor circuit. The electroacoustic efficiency of the array's piezocomposite was measured as connected with the 7-m, 34-AWG coaxial cable for the entire array and with 1-m, 28-AWG cable for three sample elements.

F. Ultrasound Driving System

256 channels of an in-house built, 512-channel ultrasound driving system were used to drive the phased array [29]. The RF signals were generated through high efficiency class D/E power converters with a DC-to-RF efficiency of 70%. This system can deliver 0 to 60 W of continuous power to each element of the array with a resolution of 0.05 W at low powers and 1 W at high powers. It can set the electrical phase to the transducer from 0 to 360° with resolution better than 2°. The system memory can hold approximately 250 preloaded phase and power settings for each array element to decrease communication bandwidth and can cycle through these settings at a rate of 18 Hz. Automatic analog phase and power feedback for individual elements were implemented to ensure proper electrical driving signals to the array. Electrical power measurements for each amplifier channel were summed to determine total electrical power for the array during array testing and the porcine experiments.

TABLE I
RELATIVE POWERS USED IN A TEMPORALLY SWITCHED FIELD WITH 24 EFFECTIVE FOCI IN A 1.0×1.0-CM^2 AREA IN THE FOCAL PLANE.

Pattern[1]	Relative Power
(b)	1.00
(c)	1.00
(d)	1.11
(e)	2.60
(f)	1.48

[1] From Fig. 2.

G. In Vivo Experiments

Five pigs ranging from 30 to 40 kg were anesthetized using an intramuscular injection (ketamine, 15 mg/kg; xylazine, 2.2 mg/kg; atropine, 0.05 mg/kg) followed by an intravenous drip to the dorsal auricular vein (ketamine, 1 mg/ml; xylazine, 1 mg/ml; guaifenesin, 50 mg/ml; 5% dextrose; rate of 2.2 ml/kg/h). The thigh skin of the pig was shaved and cleaned to create a clear acoustic window for ultrasound transmission. The pig was intubated with a 7-mm endotracheal tube to ensure an unobstructed airway. The animal protocol was approved by the Harvard Medical Area Standing Committee on Animals according to NIH and Harvard Medical School guidelines.

H. MR Experimental Set Up

The anesthetized animals were placed in the bore of a clinical 1.5-T Signa MR imager (GE Medical Systems, Millwaukee, WI) over an in-house designed and constructed 2-D positioning system that contained the array. The animal was acoustically coupled to the array through a water bath suspended above the array. A 12.5-cm diameter MR surface coil (GE Medical Systems) was placed between the array and the skin of the animal to improve the imaging signal. Prior to sonication, fast spin-echo T2-weighted images (TE/TR = 72/2000 ms, echo train length = 8, FOV = 20 cm, thickness = 3 mm, matrix size = 256×256, NEX = 2, bandwidth = 16.0 kHz) or SPGR images (SPoiled Gradient Recalled acquisition in steady state; slice thickness = 3 mm, FOV = 20 cm, TE/TR = 7.1/100 ms, echo train length = 1, NEX = 1 or 2, flip angle = 45°, bandwidth = 3.1 kHz) were used to locate the array in relation to the animal. Temperature sensitive images were taken during a nondestructive low power sonication to locate the array focus and determine the target tissue (proton resonant frequency shift constant = 0.00909 ppm/°C; slice thickness = 3 mm, matrix size = 256×128, FOV = 20 cm, scan time = 6.47 s, bandwidth = 3.1 kHz, TE/TR = 24.7/50 ms, NEX = 1, flip angle = 30°, echo train length = 1). Temperature images were then acquired during the high power ultrasound

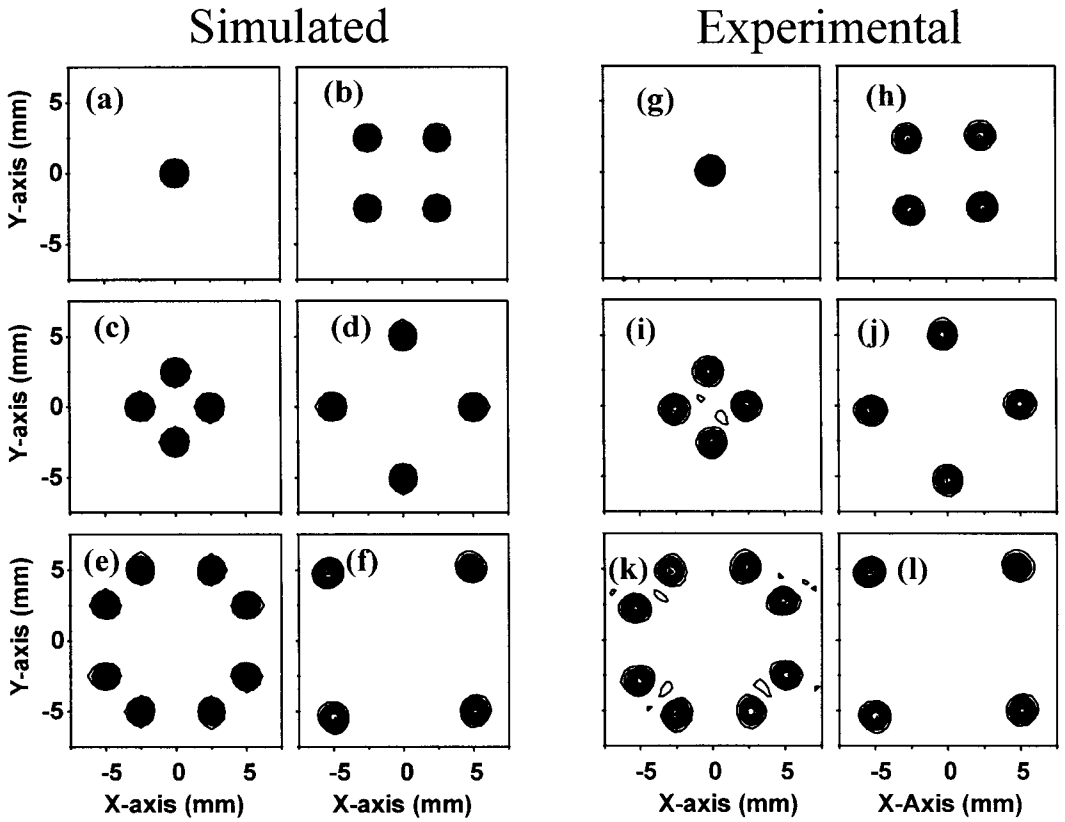

Fig. 2. Simulated (left) and corresponding hydrophone-scanned (right) intensity patterns in the focal plane used to create large focal volumes.

exposure time and during part of the cooling time (typical total imaging time of 150 s for 23 temperature images, including three images from the 20-s ultrasound exposure time). These temperature images were used to calculate the predicted thermal dose and tissue necrosis using the Sapareto and Dewey model [26], [31]. Post treatment images (T2-weighted) were taken to evaluate the tissue response and to measure tissue damage.

I. Ultrasound Surgery Experiments

The array gain [27] (defined as the sum of the intensities of the focal points divided by the total power for the array) tends to decrease significantly for patterns that contain many foci, because the creation of complex patterns can lead to increased grating lobes. Therefore, a series of multiple focus fields with ≤ 8 foci were temporally switched to fill in a large volume in the transfocal plane in the porcine experiments (see [15] for a discussion of temporal switching). The simulated acoustic patterns are found in Fig. 2. The spacing between foci in the effective grid of foci was chosen to be 2.5 mm, such that the thermal dose between foci would exceed the thermal dose threshold with a peak focal temperature below 65°C (see [32] for focal spacing simulations). The phase distribution of the array was determined using the pseudoinverse technique with a phase rotation of the desired focal pressures about the array axis to avoid axial heating [12]. The protocol used patterns (b)–(f) of Fig. 2 to fill in a volume with a 1.0×1.0-cm^2 cross section in the focal plane (24 effective foci). Table I shows the relative power levels used for the respective fields. The power levels were determined such that the focal points contained equal intensities and, therefore, approximately equal temperatures at end sonication similar to the simulations in [32]. The center focus (a) was not applied for the large volume because the thermal conduction from the other patterns would heat the center of the focal volume. The patterns were switched at a rate of 18 Hz.

III. Results

A. Acoustic Measurements

1. Radiation Force Measurements: The experimentally measured electroacoustic efficiency, maximum power, and interelement coupling measurements for the 9-element prototype and 256-element therapy array are listed in Table II. Results of the electrical L cable model estimated that 55% of the electrical power delivered to the transducer would be lost in the cable; the experimental measurements indicate that the cable loss was 58%.

2. Hydrophone Scans: Fig. 3 plots the normalized hydrophone measured focal intensity as the focus is electronically shifted along the array axis between 8 and 12 cm from the array. To demonstrate the ability to create more complex focal patterns, 16 and 25 focus fields were generated (see Fig. 4). The location of the foci is in excellent

TABLE II
ACOUSTIC POWER MEASUREMENTS OF THE 256-ELEMENT THERAPY ARRAY.

Array	Cable	Average Efficiency (%)	Maximum Acoustic Power (W/cm^2)	Coupling Decrease in Acoustic Output Power (%)
9-Element Prototype Array	1 m, 28 AWG, Belden	57%	18.1	17.8
256-Element Therapy Array	1 m, 28 AWG, Belden	64%	>9.8	not measured
256-Element Therapy Array	7 m, 34 AWG Precision Interconnect	27%	>2.5	8.9

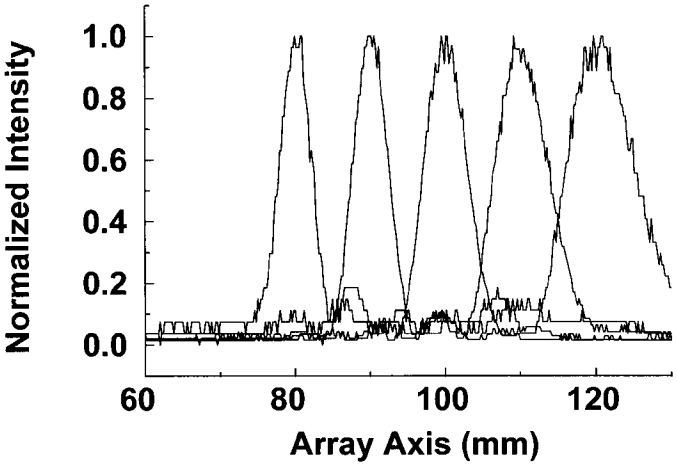

Fig. 3. Normalized intensity hydrophone measurements of a single focus scanned along the axis of the array.

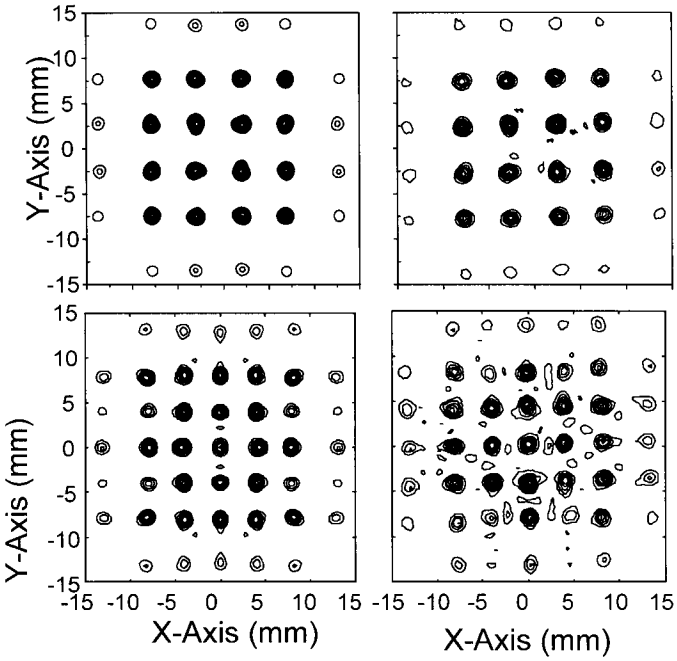

Fig. 4. Simulated (left column) and hydrophone-measured (right column) intensity field of 16- (top row) and 25- (bottom row) foci patterns created in the focal plane of the array. The individual foci were placed in a 5-mm spaced grid for the 16 foci and on a 4-mm grid for the 25 foci.

agreement; the relative amplitudes of the multiple foci vary about 20% for the 16-foci pattern and over 50% for the 25-foci pattern. The hydrophone scanned patterns that were temporally cycled to make large focal lesions are found in Fig. 2 adjacent to their corresponding simulated patterns. The peak amplitude of the foci in each of the smaller patterns varied $< 5\%$.

B. Porcine Experiments

The array was used to shift the sonication focus electronically in the porcine thigh muscle while recording temperature-sensitive MR images. Fig. 5 shows the temperature images and their corresponding simulations of a single focus that was sequentially scanned along the axis of the array. The power necessary to create in vivo temperature elevations was 1.8 to 3.5 times higher than the power predicted through simulations (see figure caption for power levels). Fig. 6 shows the T2-weighted images of the resulting lesion from the axial sonications along with the simulated and experimentally predicted lesion size. Experimentally, it measured $4.5 \times 0.7 \times 0.4$ cm^3.

Fig. 7 contains a sample of the time series of temperature images obtained during the 20-s heating and 2-min cooling period for a large focal volume (1.0×1.0-cm^2 cross section using patterns (b)–(f) of Fig. 2 with an average acoustic power of 345 W). Fig. 8 and Fig. 9 contain the spatial and temporal response of the sonication, respectively. The power level simulated was the same as the experimental power. Fig. 10 contains the post sonication T2-weighted images along with overlaying thermal dose contours predicted using the simulation data and the set of experimentally measured temperature images. Both the MR images and post mortem dissection indicated a visible coagulated lesion size of $3.2 \times 1.3 \times 1.3$ cm (5.4 cm^3) extending from 5.5 to 8.7 cm underneath the skin interface. The simulated lesion was slightly smaller. Histological examination of the lesion (hemotoxylin- and eosin-stained slides) showed fragmented muscle cells with disorganized, nonstriated cytoplasm and pyknotic nuclei consistent with other studies [33], [34]. Table III contains a summary of the large focal volume sonications. The results show significant variations in lesion size, especially at inhomogeneous tissue interfaces.

Some of the large focal volume sonications were altered by tissue interfaces. Fig. 11 shows the results of three sonications (in rows) made near the muscle interface using a

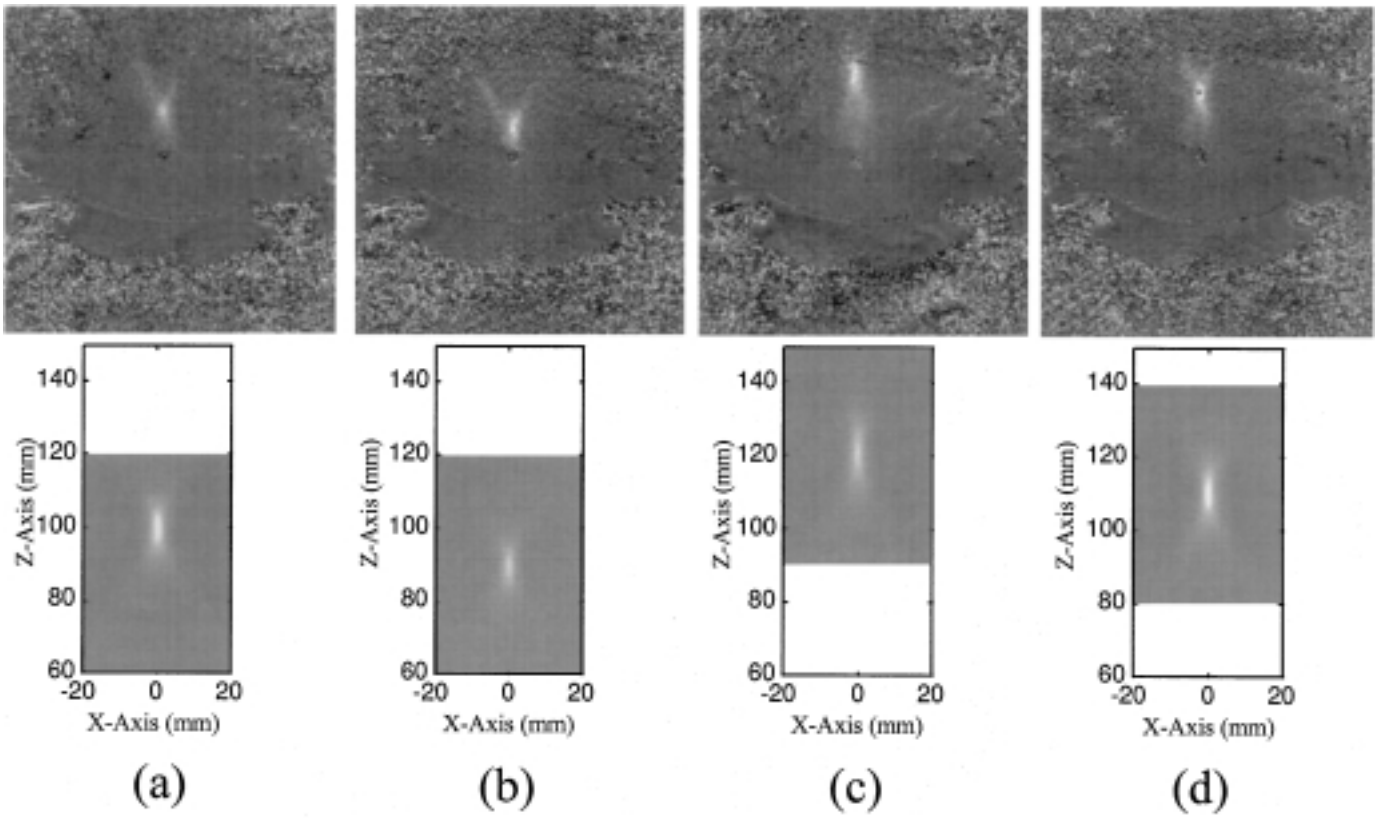

Fig. 5. Experimental temperature images (top) and simulated temperature contours (bottom) of on-axis electronic shifting of a single focus. The sequential sonications from left to right were placed at a distance of 10, 9, 12, and 11 cm from the transducer, which was placed 3 cm from the skin of the porcine thigh. The peak temperature elevations were measured to be 37, 27, 27, and 38°C from left to right for input powers of 61, 61, 146, and 85 W, respectively. The simulated fields were driven such that their peak temperature matched the experimental results. The simulated powers were 34, 23, 41, and 38 W from left to right.

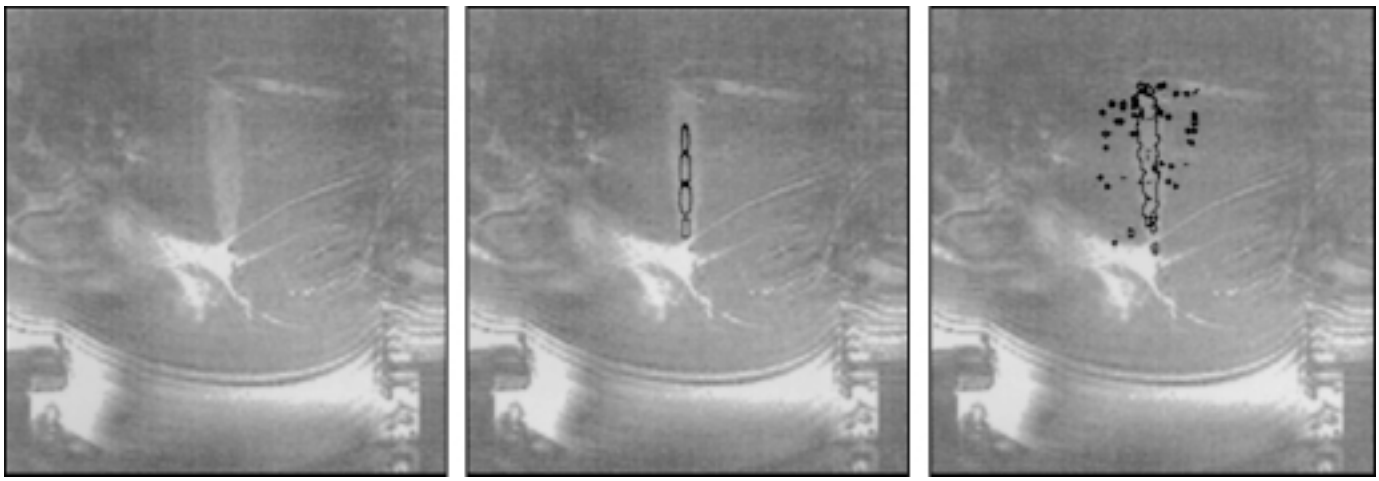

Fig. 6. Lesion produced from the axial-shifted sonications of Fig. 5. The middle image overlays the simulated predicted lesion size corresponding to a thermal dose of 240 equivalent min at 43°C. The right image shows the predicted lesion using the temperature images obtained during sonication and cooling applied to the Sapareto and Dewey model [25], [31] (same thermal dose level).

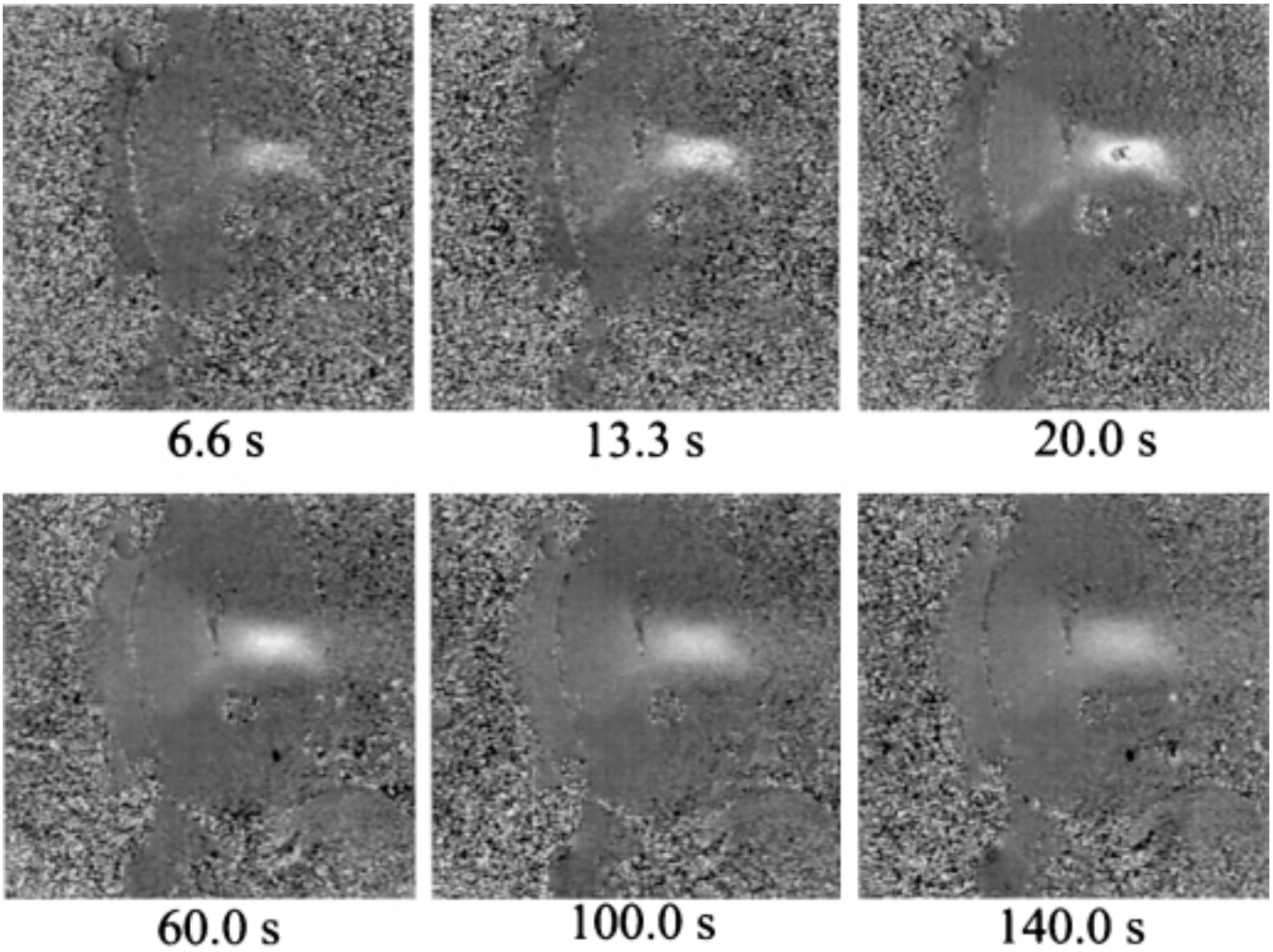

Fig. 7. Series of temperature images along the array axis during a 20-s sonication period (top) and during the first 2 min of the cooling period (bottom). The array is still underneath the porcine thigh, although the orientation of the MR images places the array on the left as sonicating from left to right.

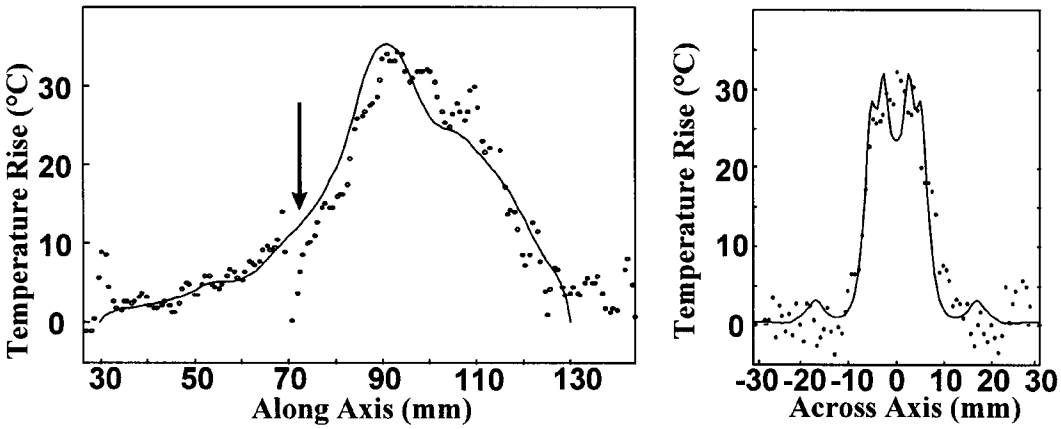

Fig. 8. End sonication spatial temperature response of the 1.0×1.0-cm^2 cross section focus. The solid line corresponds to the simulated temperature response, and the circles correspond to the MR measured temperature elevations. The arrow indicates the location of muscle interface tissue where the MR signal does not correlate with temperature.

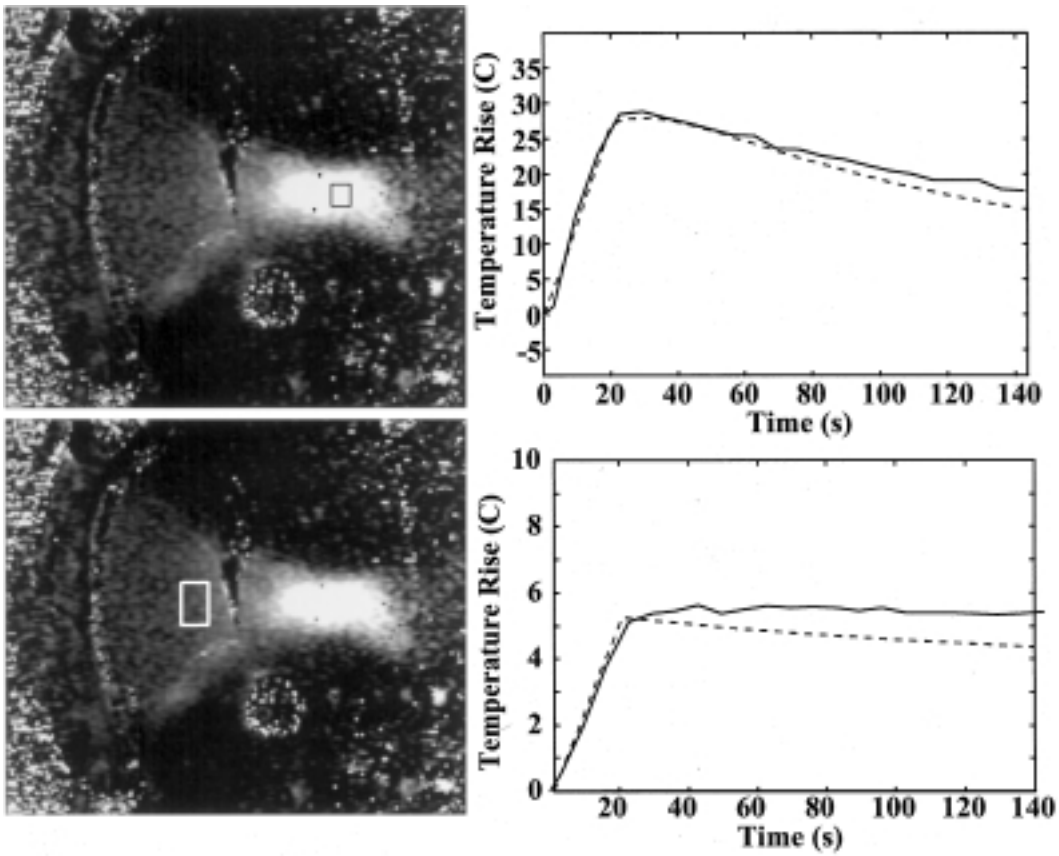

Fig. 9. Temperature elevations at end sonication in the focus (top) and in the prefocal tissue (bottom). The time plots on the right correspond to the simulated (dashed) and experimental (solid) average temperature in the boxes overlaying the respective images on the right.

TABLE III

SUMMARY OF LARGE FOCAL LESIONS WITH THE EXCEPTION OF THE 10 OVERLAPPING LARGE VOLUME SONICATIONS.

#	Average Acoustic Power (W)	Lesion depth (cm from skin)	MR measured dimensions (cm^3)	Volume (cm^3)	Peak Temperature Elevation (°C)
1	172 (40 s)	2	$3.2 \times 1.2 \times 1.2$	4.6	32
2	172 (20 s)	-	no lesion	0	20
3	259 (20 s)	4.2	round 1.1	0.69	22
4	259 (20 s)	5.1	$3.1 \times 1.2 \times 1.2$	4.4	24.5
5	259 (20 s)	4.8	$2.9 \times 1.1 \times 1.1$	3.5	20
6	302 (20 s)	5.2	$3.1 \times 1.4 \times 1.2$	5.2	26.1
7	259 (20 s)	5.1	$3.1 \times 1.2 \times 1.2$	4.4	33.1
8	259 (20 s)	4.9	$2.9 \times 1.0 \times 1.0$	2.9	27.6
9	302 (20 s)	5.5	$2.5 \times 1.1 \times 1.0$	2.7	20
10	259 (20 s)	-	no lesion	0	17
11	259 (20 s)	-	lesion at prefocal muscle interface	0	10
12	345 (20 s)	5.5	$3.4 \times 1.2 \times 1.2$	4.9	35
13	345 (20 s)	5.5	$2.7 \times 0.9 \times 0.9$	2.1	24.6

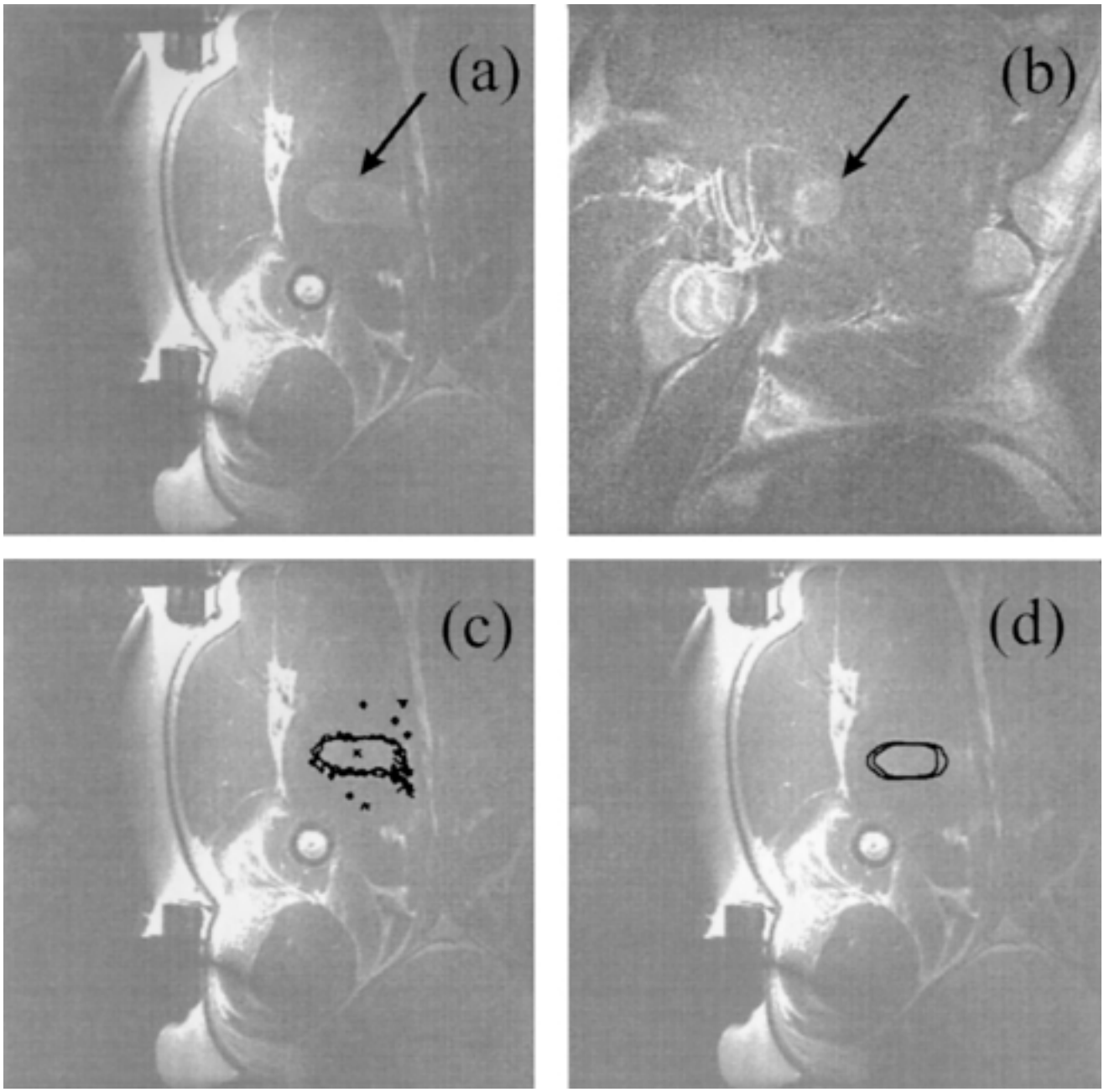

Fig. 10. T2-weighted images of lesion in thigh. Image (a) is along the axis of the array, and image (b) is in the focal plane. Images (c) and (d) are the along axis image with overlaying thermal dose contours corresponding to 240 and 2000 equivalent min at 43°C using the experimentally measured temperature images (c) and simulated temperature field (d).

large focal volume protocol with > 30 min between successive sonications. From left to right, the images show the end sonication temperature image, a T2-weighted image with experimentally estimated dose contours of 240 and 2000 equivalent min at 43°C, and a T2-weighted image of the produced lesion. The average temperature elevation in the muscle just under the skin surface was measured from the MR images to be 2.2, 2.5, and 2.3°C, respectively, verifying that similar power levels were delivered through the skin for each of the sonications. The peak temperature in the focal zone was measured as 33.1, 15.2, and 14.7°C (from top to bottom), indicating that the ability to focus at the set depth was compromised for the later two sonications. The first row of images shows a lesion, the shape of which is skewed near the interface. The second row of images shows a lesion that is barely visible and not well formed. The third row of images shows a nondistinct lesion beyond the interface and a definite lesion in front of the interface.

A series of 10 adjacent large focal volumes were performed in the thigh of one pig. The average acoustic power was 345 W (Table I). After each sonication, the array was moved 7.5 mm. Each sonication lasted 20 s, and there was an average of 9 min between consecutive sonications.

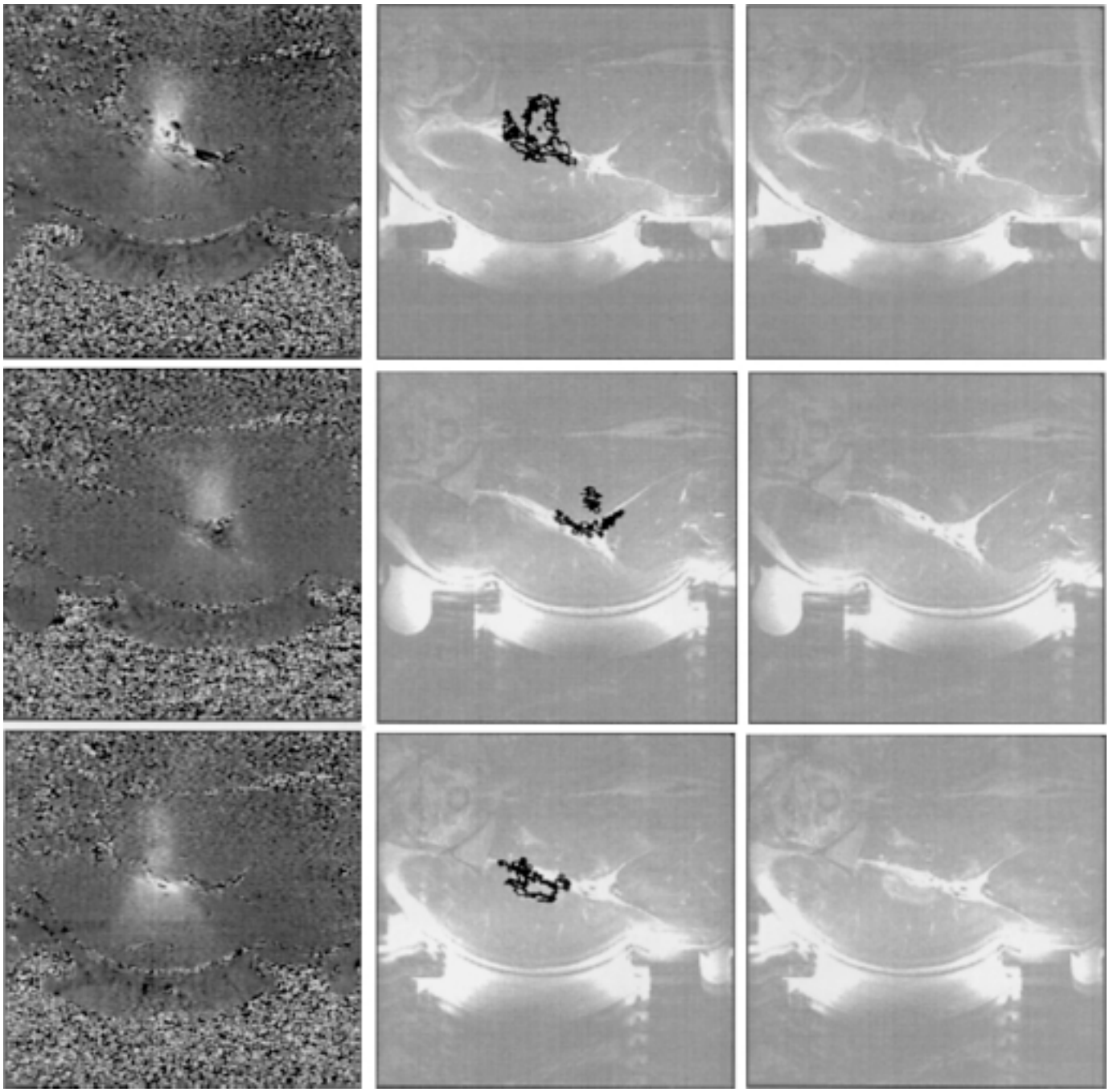

Fig. 11. Three large focal region sonications close to a muscle interface. The focal pattern covered a 1.0×1.0- cm^2 area in the focal plane of the array. The average acoustic power for each of the sonications was 259 W. The images on the left are the temperature images at peak temperature, the center images are the T2 images of the lesion with overlying thermal dose contours, and the right images are the T2 lesion images without the contours.

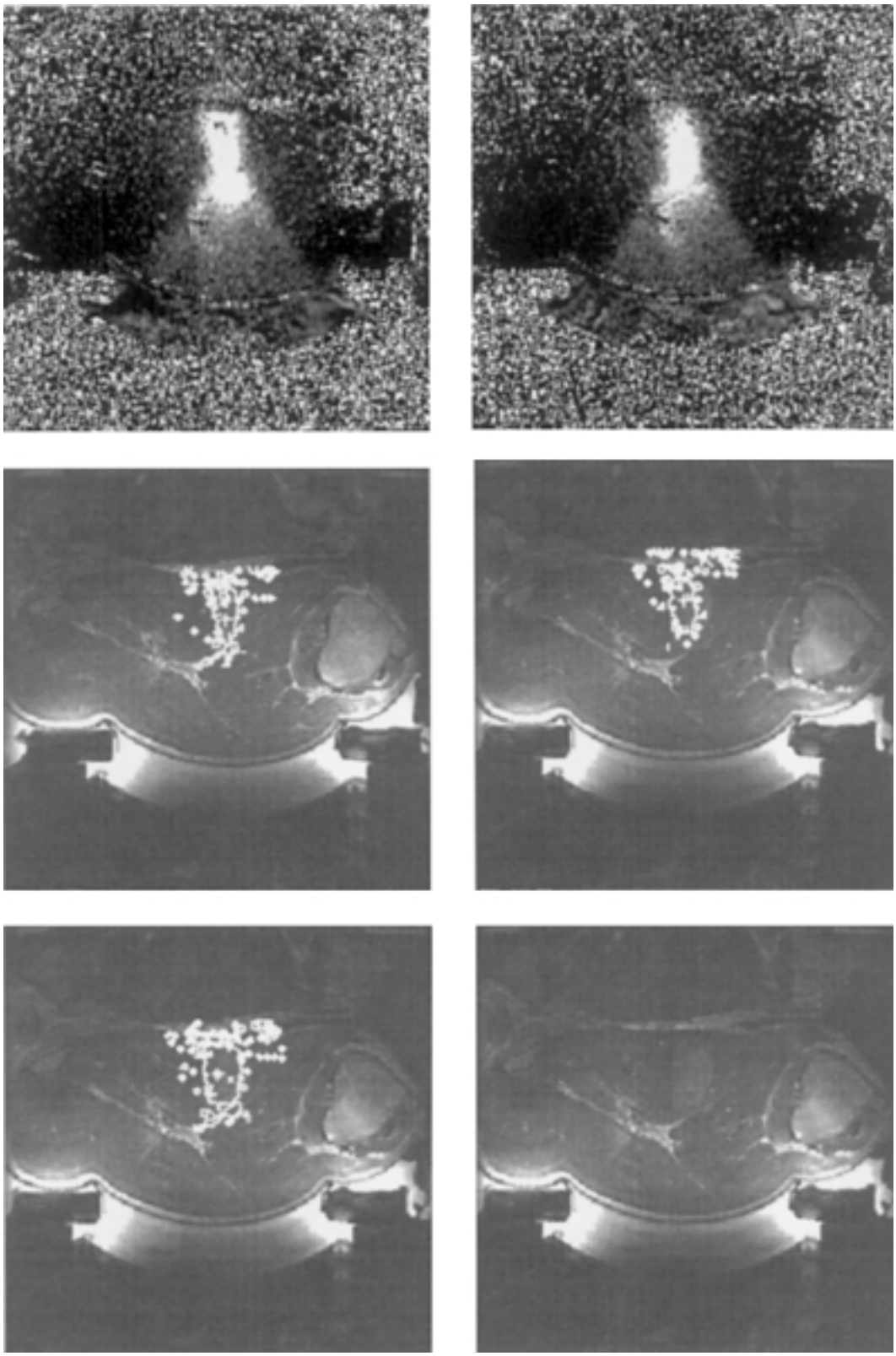

Fig. 12. Images of the first (left) and second (right) sonication of the 10 overlapping ultrasound exposures. The top images are the MR temperature images at end sonication. The middle images contain the resulting T2-weighted image with overlapping thermal dose contours of 240 equivalent min at 43°C estimated using the MR temperature images. The bottom images contain the resulting T2-weighted images with and without the cumulative thermal dose contour.

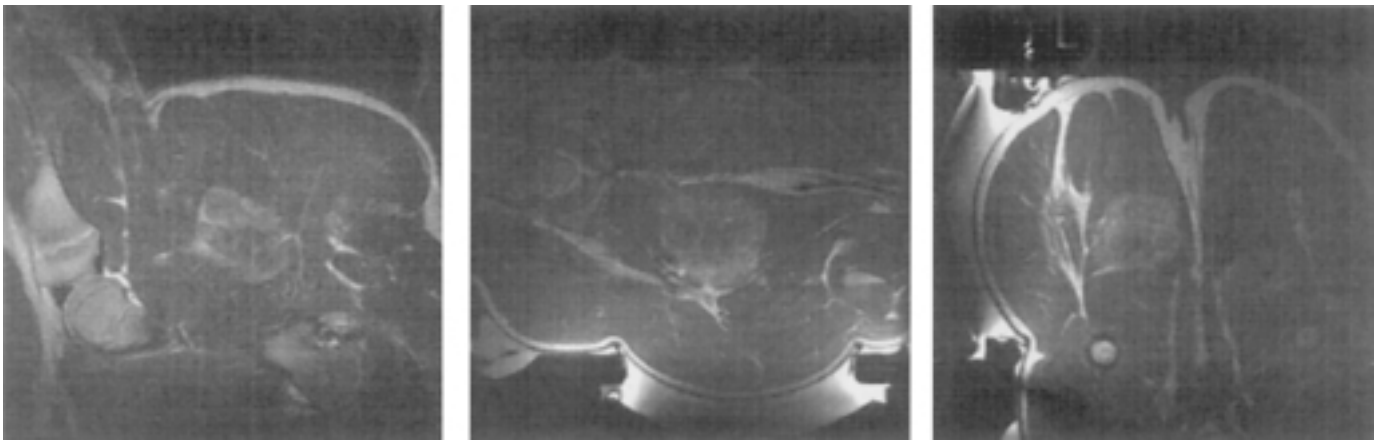

Fig. 13. T2 images of lesion formed by two rows of five large volume sonications. The images are taken in three planes of the rectangular lesion shape. According to the MR images, the lesion measures $3.8 \times 2.2 \times 3.0$ cm^3 (25 cm^3).

Fig. 12 shows the temperature response and lesion formed for the first two sonications. Fig. 13 is a T2-weighted image of the complete lesion. It measured $3.8 \times 2.2 \times 3.0$ cm^3 (25 cm^3). On gross examination, the lesion was the same size.

IV. Discussion

Overall the 256-element array demonstrated both in acoustic tests and in vivo experiments the advantages of a large scale phased array. It was able to shift both individual and sets of foci electronically. The hydrophone scans proved that a large phased array can construct field patterns accurately with up to 16 foci without causing excessive grating lobes and with up to 25 foci with less accuracy. There was good agreement among all of the simulated and hydrophone scanned fields of lesser numbers of foci.

The 1-3 piezocomposite material offers a practical alternative to diced PZT pseudocrystals in the construction of large scale therapeutic arrays. The material is robust and has withstood over 100 h of submersion in water during therapy sessions. The transducer array was able to produce up to 350 W of acoustic power despite its low electroacoustic efficiency through its lengthy cables. However, both the 9-element prototype array and the 256-element therapy array suffer from significant interelement coupling at therapeutic powers. The acoustic efficiency measurements of adjacent elements indicate that high power interelement coupling can cause significant changes in acoustic output power from the array. Nevertheless, although inter-element coupling can decrease array output significantly, the acoustic output power levels are still sufficient for most therapeutic specifications.

A comparison between the acoustic measurements of the prototype and therapy arrays indicate that an acoustic quarter wave matching layer may not offer significant advantages in a piezocomposite monofrequency therapeutic array. The electroacoustic efficiency of the array without the matching layer is higher than the array with the matching layer. Because the arrays are air-backed, it is believed that the loss in the piezomaterial from multiple wave reflections is less than the transmission loss in the matching layer. More importantly, the acoustic matching layer significantly increased the undesirable inter-element coupling. In our experiments, the main advantage of using a matching layer was to protect the ground electrode of the array.

A total of 29 sonication lesions was produced in the thigh muscles, including 20 that were produced from the large focal volume sonication. The thigh experiments indicate that large (>5 cm^3), deep seated lesions can be created in vivo in a single sonication, verifying the simulation studies by [14], [19]. Although the lesions can be created in a 20-s sonication time, it would be misleading to say that the tumor treatment rate is $> 5/20 = 0.25$ cm^3/s because there is a significant cooling time necessary before an adjacent sonication can occur ($>$ 5 min). As demonstrated by simulations for phased arrays [9] and experimental results for single focus transducers [35]–[37], the cooling time is necessary to avoid excessive near field heating, accumulation of thermal dose, and undesirable boiling of water in the prefocal tissue. The MR temperature images indicate the long period needed to cool near field tissue following a large focal volume ultrasound exposure in low perfused tissue. Tissues with higher perfusion could have dramatically shorter cooling periods. The overlapping sonications in the thigh, however, showed that $>$ 25 cm^3 could be treated in $<$ 90 min. However, the interval between sonications used in this experiment might have been longer than required.

No lesion was formed in the focal plane for 3 of the large volume, high power sonications. This was predicted by the MR temperature images. In each case, a muscle interface appeared to block the ultrasound transmission such that there was little or no measurable temperature rise beyond the interface. The temperature images of Fig. 11 help explain the variable results. In the first sonication, the interface appears to have caused some beam distortion (possibly refraction) and some heating near the interface, leading to a lesion with a bent shape with a wider region near the interface. The temperature image of the second

sonication indicates a wide, diffuse focal region after the ultrasound passed through the interface. The enlarged focal region led to a lower average temperature and a less distinguishable coagulation volume. The third row of the images indicate that the transducer side of the interface was heated to high temperatures, leading to a pre-interface lesion. It is possible that cavitation was produced in the interface causing the excessive temperatures and a significant decrease in energy transmitted beyond the interface (a method to detect cavitation was not employed in this sonication). Interface-related cavitation events have been demonstrated earlier [33], [38]. In each case, the temperature images taken during sonication still accurately predict the T2-weighted image measurements of lesion volume in the muscle, although the accuracy of the temperature images at the interface is compromised by the lack of MR signal in fatty tissue.

The experimentally measured temperature and the estimated thermal dose response using the MR scanner correlated very well with the simulated temperature distribution for the large focal volume sonications in homogeneous media. The same simulated and experimental power level yielded almost identical peak temperatures. The difference between the simulated and measured temperature during cooling is most likely a result of the simulated perfusion being too high (1 kg/m^3/s). In the case of single focus sonications (such as the axial scanning presented in this paper), there is a significant difference (up to a factor of three) between the power level simulated and experimentally tested power to produce the same temperature rise. This is similar to the results found in dog thigh muscle [23], which indicated that the peak intensity of a single focus beam was more highly attenuated than the total power of the beam. This was attributed to possible scattering and refraction of the beam. The large focal volume sonications in this study did not demonstrate this same result; therefore, the model used in this study performs better for large focal volumes than the small volumes produced by single focus transducers. This is in agreement with the results from Fjield [39].

The in vivo thigh muscle experiments also demonstrated that a well-constructed and driven phased array transducer can be controlled accurately without invasive acoustic feedback measures at clinically significant depths. Lesions much larger than the volume of a single focus lesion were produced at depths of 8 cm below the skin. This is deep enough for almost all extremity treatments, breast tumor treatments, and kidney treatments, and it would be enough for some liver mass treatments.

Lastly, the experiments again confirm the in vivo utility of temporal multiplexing multiple focus patterns in the target volume during a short sonication. A multiple focus pattern with excessive numbers of foci can decrease the sharp focal intensities and thermal gradients needed in the focal plane of the transducer. Large numbers of foci can also lead to increased grating lobes as in the case of the 25-foci pattern. Therefore, a larger pattern of foci is formed more effectively by using several smaller patterns of foci that are rapidly cycled during sonication. The ability to switch between phase and power distributions rapidly is an important consideration when evaluating the driving hardware for a therapeutic array [29]. This technique can also be used to optimize the thermal dose delivered to large tissue volumes and further decrease treatment time and average power needed from the array.

V. Conclusion

This research has shown the feasibility and advantage of using a large scale ultrasound phased array in vivo for MR guided ultrasound coagulation of large volumes of deep seated tissue. The phased array offers a control and flexibility not available in single focus transducers or in arrays with fewer elements. In addition, the theoretical model used in this research has been shown to model the response of large focal volumes accurately when large interfaces are not close to the focal volume. This study has also confirmed the ability of MR to detect lesion forming temperature elevations and determine treatment effectiveness post sonication for lesions at clinically significant depths. In a clinical setting, the advances in control will make patient treatment more accurate as well as more clinically feasible.

Acknowledgment

The authors thank GE Medical Systems for the temperature imaging sequence.

Appendix A

A. Pressure Calculations for the Phased Array [22]

The pressure field from an ultrasound element through a lossy substrate can be modeled as:

$$p(\mathbf{r}) = \frac{i\rho_o ck}{2\pi}\int_A \frac{e^{ik(\mathrm{r}-\mathrm{r}')}e^{-\mu d}u}{\mathbf{r}-\mathbf{r}'}dA$$

where ρ_o is the tissue density, c is the speed of sound, k is the wavenumber ($2\pi/\lambda$ where λ is the ultrasonic wavelength), r is the coordinate vector (x, y, z) of the pressure point, r' is the coordinate vector of the incremental source area of the complete transducer area A, μ is the attenuation coefficient in the lossy material (absorption and scattering), d is the ray distance in the lossy material between the source point and the location of the desired pressure point, and u is the complex surface velocity of that source (magnitude and phase). For an array with N elements, the pressure at a given point m corresponding to a location (x_m, y_m, z_m) is given by:

$$p_m = \sum_{n=1}^{N}\frac{i\rho ck}{2\pi}\int_A \frac{e^{-ikr_{mn}}e^{-\mu d}u_n}{r_{mn}}dA$$

where subscript n denotes parameters associated with the nth element of the array. This model neglects temperature, non-linear, refraction, and scattering effects on pressure calculation (scattering attenuation lumped with absorption).

B. Pseudoinverse Technique [27]

The pressure at a set of points can be derived from a transfer function h_{mn} equal to

$$h_{mn} = \frac{i\rho ck}{2\pi} \int_A \frac{e^{-ikr_{mn}} e^{-\mu d}}{r_{mn}} dA$$

such that

$$p = Hu$$

where p is an $m \times 1$ vector corresponding to a set of pressures at m different spatial locations, H is the $m \times n$ transfer matrix, and u is the $n \times 1$ vector corresponding to the driving velocities. This matrix can be inverted such that given a set of desired pressures at given locations, the driving signals can be calculated. This can be accomplished using the pseudoinverse. The matrix form of the transfer function can be written as:

$$H = XSY^*$$

where X and Y are unitary matrices and S is a rectangular matrix with diagonal elements corresponding to the eigenvalues of H. The pseudoinverse is then given by

$$H^+ = Y\hat{S}X^*$$

where $^+$ indicates pseudoinverse, * indicates the complex conjugate transpose, and $\hat{S}$ is formed from S with the diagonal elements replaced by their reciprocal.

C. Intensity and Specific Absorption Rate Calculations [40]

The time average power absorbed $\langle q \rangle$ by the tissue at location (x, y, z) (when the effects of shear viscosity are small for a CW, monofrequency signal) can be modeled as

$$\langle q(x, y, z) \rangle = \alpha \frac{p^2(x,\ y,\ z)}{\rho_o v}$$

where α is the absorption coefficient, ρ_o is the tissue density, and v is the speed of sound in the tissue.

D. Bioheat Transfer Equation [25]

The tissue temperature response can be simulated using the bio-heat transfer equation:

$$\rho_o c_t \frac{dT(x, y, z, t)}{dt} = k\nabla^2 T(x, y, z, t) - wc_b(T(x, y, z, t) - T_a) + \langle q(x, y, z, t) \rangle$$

where ρ_o is the tissue density, c_t is the specific heat of the tissue, c_b is the specific heat of the blood, k is the thermal conductivity, w is the perfusion, T_a is the arterial blood temperature, and $T(x, y, z, t)$ is the temperature at location (x, y, z) at time t. ∇^2 is the spatial gradient, and d/dt is the time derivative.

E. Thermal Dose Calculation [26]

The thermal lesions are predicted using the Sapareto Dewey model:

$$D(t) = \int_0^t R^{T(t) - T_{\text{ref}}} dt_1$$

where $R = 2$ if $T(t) > 43°\text{C}$, 4 if $T(t) < 43°\text{C}$. $T(t)$ corresponds to the tissue temperature as a function of time, and $D(t)$ corresponds to the accumulated thermal dose (units of equivalent minutes at a given temperature). The threshold for lesion production is between 20 and 240 equivalent min at 43°C.

References

[1] G. R. ter Haar, D. Sinnett, and I. Rivens, "High intensity focused ultrasound - a surgical technique for the treatment of discrete liver tumors," *Phys. Med. Biol.*, vol. 34, pp. 1743–1750, 1989.

[2] W. J. Fry, J. W. Barnard, F. J. Fry, R. F. Krumins, and J. F. Brennan, "Ultrasonic lesions in the mammalian central nervous system," *Science*, vol. 122, pp. 517–518, 1955.

[3] W. J. Fry and F. J. Fry, "Fundamental neurological research and human neurosurgery using intense ultrasound," *IRE Trans. Med. Electron.*, vol. ME-7, pp. 166–181, 1960.

[4] C. A. Linke, E. L. Carstensen, L.A. Frizzell, A. Elbadawi, and C. W. Fridd, "Localized tissue destruction by high-intensity focused ultrasound," *Arch. Surg.*, vol. 107, pp. 887–891, 1973.

[5] J. E. Zimmer, K. Hynynen, D. S. He, and F. I. Marcus, "The feasibility of using ultrasound for cardiac ablation," *IEEE Trans. Biomed. Eng.*, vol. 42, pp. 891–897, 1995.

[6] G. Vallancien, M. Harouni, B. Veillon, A. Mombet, D. Prapotnich, J. M. Bisset, and J. Bougaran, "Focused extracorporeal pyrotherapy: Feasibility study in man," *J. Endourol.*, vol. 6, pp. 173–180, 1992.

[7] R. Yang, N. T. Sanghvi, F. J. Rescorla, K. K. Kopecky, and J. L. Grosfeld, "Liver cancer ablation with extracorporeal high-intensity focused ultrasound," *Eur. Urol.*, vol. 23 (Suppl. 1), pp. 15–22, 1993.

[8] F. Prat, J. Y. Chapelon, A. Fadil, A. Sibille, Y. Theilliere, T. Ponchon, and D. Cathignol, "Focused liver ablation by cavitation in the rabbit: a potential new method of extracorporeal treatment," *Gut*, vol. 35, pp. 395–400, 1994.

[9] X. Fan and K. Hynynen, "Ultrasound surgery using multiple sonications - treatment time considerations," *Ultrason. Med. Biol.*, vol. 22, pp. 471–482, 1996.

[10] C. A. Cain and S. A. Umemura, "Concentric-ring and sector vortex phased array applicators for ultrasound hyperthermia therapy," *IEEE Trans. Microwave Theory Tech.*, vol. 34, pp. 542–551, 1986.

[11] E. S. Ebbini, S.-I. Umemura, M. Ibbini, and C. Cain, "A cylindrical-section ultrasound phased array applicator for hyperthermia cancer therapy," *IEEE Trans. Ultrason., Ferroelect., Freq. Contr.*, vol. 35, pp. 561–572, 1988.

[12] X. Fan and K. Hynynen, "Control of the necrosed tissue volume during noninvasive ultrasound surgery using a 16 element phased array," *Med. Phys.*, vol. 22, pp. 297–308, 1995.

[13] S. A. Goss, L. A. Frizzell, J. T. Kouzmanoff, J. M. Barich, and J. M. Yang, "Sparse random ultrasound phased array for focal surgery," *IEEE Trans. Ultrason., Ferroelect., Freq. Contr.*, vol. 43, pp. 1111–1121, 1996.

[14] H. Wan, P. VanBaren, E.S. Ebbini, and C.A. Cain, "Ultrasound surgery: Comparison of strategies using phased array systems," *IEEE Trans. Ultrason., Ferroelect., Freq. Contr.*, vol. 43, pp. 1085–1098, 1996.

[15] D. R. Daum and K. Hynynen, "Optimization of thermal dose using switching mode patterns of a spherically shaped square element phased array," in *1996 IEEE Ultrason. Symp. Proc.*, New York, NY, pp. 1309–1312.
[16] T. Fjield, X. Fan, and K. Hynynen, "A parametric study of the concentric-ring transducer design for MRI guided ultrasound surgery," *J. Acoust. Soc. Amer.*, vol. 100, pp. 1220–1230, 1996.
[17] T. Fjield and K. Hynynen, "The combined concentric-ring and sector-vortex phased array for MRI guided ultrasound surgery," *IEEE Trans. Ultrason., Ferroelect., Freq. Contr.*, vol. 44, pp. 1157–1167, 1997.
[18] K. Hynynen, A. Chung, T. Fjield, M. T. Buchanan, D. R. Daum, V. Colucci, P. Lopath, and F. Jolesz, "Feasibility of using ultrasound phased arrays for MRI monitored noninvasive surgery," *IEEE Trans. Ultrason., Ferroelect., Freq. Contr.*, vol. 43, pp. 1043–1053, 1996.
[19] X. Fan and K. Hynynen, "A study of various parameters of spherically curved phased arrays for noninvasive ultrasound surgery," *Phys. Med. Biol.*, vol. 41, pp. 591–608, 1996.
[20] E. S. Ebbini and C. A. Cain, "A spherical-section ultrasound phased array applicator for deep localized hyperthermia," *IEEE Trans. Biomed. Eng.*, vol. 38, pp. 634–643, 1991.
[21] C. Damianou and K. Hynynen, "Near-field heating during pulsed high temperature ultrasound hyperthermia treatment," *Ultrason. Med. Biol.*, vol. 19, pp. 777–787, 1993.
[22] J. Zemanek, "Beam behavior within the nearfield of a vibrating piston," *J. Acoust. Soc. Amer.*, vol. 49, pp. 181–191, 1971.
[23] E. G. Moros and K. Hynynen, "A comparison of theoretical and experimental ultrasound field distributions in canine muscle tissue *in vivo*," *Ultrason. Med. Biol.*, vol. 18, pp. 81–95, 1992.
[24] F. A. Duck and M. A. Perkins, "Amplitude-dependent losses in ultrasound exposure measurement," *IEEE Trans. Ultrason., Ferroelect., Freq. Contr.*, vol. 35, pp. 232–241, 1988.
[25] H. H. Pennes, "Analysis of tissue and arterial blood temperatures in the resting human forearm.," *J. Appl. Physiol.*, vol. 1, pp. 93–122, 1948.
[26] S. A. Sapareto and W. C. Dewey, "Thermal dose determination in cancer therapy," *Int. J. Radiat. Oncol. Biol. Phys.*, vol. 10, pp. 787–800, 1984.
[27] E. S. Ebbini and C. A. Cain, "Multiple-focus ultrasound phased-array pattern synthesis: Optimal driving-signal distributions for hyperthermia," *IEEE Trans. Ultrason., Ferroelect., Freq. Contr.*, vol. 36, pp. 540–548, 1989.
[28] H. F. Stewart. "Ultrasonic measurement techniques and equipment output levels," in *Essentials of Medical Ultrasound: A Practical Introduction to the Principles, Techniques, and Biomedical Applications*, M. H. Repacholi and D. A. Benwell, Eds. Clifton, NJ: Humana Press, 1982. pp. 77–116.
[29] D. R. Daum, M. T. Buchanan, T. Fjield, and K. Hynynen, "Design and evaluation of a feedback based phased array system for ultrasound surgery," *IEEE Trans. Ultrason., Ferroelect., Freq. Contr.*, vol. 45, pp. 431–438, 1998.
[30] E. M. Anderson, *Electric Transmission Line Fundamentals*, Reston, VA: Prentice Hall, 1995.
[31] A. Chung, K. Hynynen, H. E. Cline, and F. A. Jolesz, "Quantification of thermal exposure using proton resonance frequency shift," *Proc. SMR 4th Meeting*, p. 1751, 1996.
[32] D. R. Daum and K. Hynynen, "A theoretical design model for ultrasound surgery using a spherically-sectioned phased array," in *Proc. 1997 IEEE Ultrason. Symp.*, Toronto, Canada.
[33] K. Hynynen, A. Darkazanli, E. Unger, and J. F. Schenck, "MRI-guided noninvasive ultrasound surgery," *Med. Phys.*, vol. 20, pp. 107–115, 1993.
[34] K. Hynynen, A. Darkazanli, C. Damianou, E. Unger, and J. F. Schenck, "The usefulness of contrast agent and GRASS imaging sequence for MRI guided noninvasive ultrasound surgery," *Invest. Radiol.*, vol. 29, pp. 897–903, 1994.
[35] C. A. Damianou and K. Hynynen, "Focal spacing and near-field heating during pulse high temperature ultrasound therapy," *Ultrason. Med. Biol.*, vol. 19, pp. 777–787, 1993.
[36] A. L. Malcolm and G. R. ter Haar, "Ablation of tissue volumes using high intensity focused ultrasound," *Ultrason. Med. Biol.*, vol. 22, pp. 659–669, 1996.
[37] N. McDannold, F. A. Jolesz, and K. Hynynen, "The determination of the optimal delay between sonications during focused ultrasound surgery using MRI to monitor thermal build-up in vivo," *Radiology*, vol. 211, pp. 419–426, 1999.
[38] K. Hynynen, "The threshold for thermally significant cavitation in dog's thigh muscle in vivo," *Ultrason. Med. Biol.*, vol. 17, pp. 157–169, 1991.
[39] T. Fjield, N. McDannold, C. Silcox, and K. Hynynen, "In vivo verfication of the acoustic model used to predict temperature elevations for MRI guided ultrasound surgery," in *Proc. 1998 IEEE Int. Ultrason. Symp.*, Sendai, Japan, pp. 14–15.
[40] K. Hynynen. "Biophysics and technology of ultrasound hyperthermia." *Methods of External Hyperthermic Heating*, M. Gautherie, Ed. New York: Springer-Verlag, 1990, pp. 61–115.
[41] T. H. Mulligan, D. Lynch, J. M. Mulvin, J. M. Greene, J. M. Smith, and J. M. Fitzpatrick, "High intensity focused ultrasound in the treatment of benign prostatic hyperplasia," *Br. J. Urol.*, vol. 79, pp. 177–180, 1998.
[42] K. Nakamura, S. Baba, S. Saito, M. Tachibana, and M. Murai, "High-intensity focused ultrasound energy for benign prostatic hyperplasia: clinical response at 6 months to treatment using Sonablate 200(tm)," *J. Endourology*, vol. 11, pp. 197–201, 1997.
[43] S. Madersbacher, M. Pedevilla, L. Vingers, M. Susani, and M. Marberger, "Effect of high-intensity focused ultrasound on human prostate cancer in vivo," *Cancer Res.*, vol. 55, pp. 3346–3351, 1995.
[44] D. J. Coleman, F. L. Lizzi, J. Driller, A. L. Rosado, S. Chang, T. Iwamoto, and D. Rosenthal, "Therapeutic ultrasound in the treatment of glaucoma," *Ophthalmology*, vol. 92, pp. 339–346, 1985.
[45] G. Vallancien, M. Harouni, B. Veillon, A. Mombet, D. Prapotnich, J. M. Bisset, and J. Bougaran, "Focused extracorporeal pyrotherapy: Feasibility study in man," *J. Endourology*, vol. 6, pp. 173–180, 1993.
[46] A. Gelet, J. Y. Chapelon, J. Margonari, Y. Theillere, F. Gorry, R. Souchon, and R. Bouvier, "High-intensity focused ultrasound on human benign prostatic hypertrophy," *Eur. Urol.*, vol. 23, pp. 44–47, 1993.
[47] S. Madersbacher, C. Kratzik, N. Szabo, M. Susani, L. Vingers, and M. Marberger, "Tissue ablation in bennig prostatic hyperplasia with high intensity focused ultrasound," *Eur. Urol.*, vol. 23, pp. 39-43, 1993.
[48] R. Bihrle, R. S. Foster, N. T. Sanghvi, F. J. Fry, and J. P. Donohue, "High-intensity focused ultrasound in the treatment of prostate tissue," *J. Urology*, vol. 43 (Suppl.), pp. 21–26, 1994.

Douglas R. Daum was born in Wilmington, DE, on December 29, 1968. He received the B.S. and M.S. degrees in electrical engineering from Brigham Young University in 1993 and 1994, respectively. He is currently a candidate for the Ph.D. degree in medical engineering in the Harvard/M.I.T. Division of Health Sciences and Technology, Cambridge, MA.

His current research interests are in the therapeutic application of phased array ultrasound.